Jing et al. Geoscience Letters (2024) 11:2
https://doi.org/10.1186/s40562-023-00317-3

Geoscience Letters

RESEARCH LETTER Open Access

Use of GOCI-II images for detection of harmful algal blooms in the East China Sea

Yutao Jing[1,2], Chi Feng[3*], Taisheng Chen[2,3], Yuanli Zhu[4,5], Changpeng Li[6], Bangyi Tao[6] and Qingjun Song[7]

Abstract

The East China Sea (ECS) has experienced severe harmful algal blooms (HABs) that have deleterious ecological effects on marine organisms. Recent studies indicated that deploying of a second geostationary ocean color imager (GOCI-II) can significantly improve ocean monitoring. This study systematically assessed GOCI-II and its ability to detect HABs and distinguish between dinoflagellates and diatoms in the ECS. First, the remote-sensing reflectance ($R_{rs}(\lambda)$, λ represents the wavelength) obtained from GOCI-II was compared to the local measurement data. Compared to the bands at 412 and 443 nm, the bands at 490, 510, and 620 nm exhibited excellent consistency, which is important for HAB detection. Second, four different methods were employed to extract bloom areas in the ECS: red tide index (RI), spectral shape (SS), red band line height ratio (LHR), and algal bloom ratio (R_{AB}). The SS (510) algorithm was the most applicable for detecting blooms from GOCI-II imagery. Finally, the classification capability of GOCI-II for dinoflagellates and diatoms was evaluated using three existing algorithms: the bloom index (BI), combined *Prorocentrumdonghaiens* index (PDI) and diatom index (DI), and the spectral slope ($R_{\_slope}$). The BI algorithm yielded more satisfactory results than the other algorithms.

Keywords Bloom detection, GOCI-II, Harmful algal blooms, Remote sensing reflectance, East China Sea

Introduction

Harmful algal blooms (HABs) are abnormal occurrences characterized by a rapid increase in phytoplankton in marine ecosystems. HAB organisms produce toxins that may result in the death of various marine species (Lu et al. 2005; Tang et al. 2006; Zhao et al. 2009). HABs are ecological disasters that disrupt the balance of marine ecosystems, deteriorate water quality, and cause environmental pollution. Furthermore, HABs significantly affect human health and economic activities (Hallegraeff et al. 2003; Zohdi and Abbaspour 2019).

In recent decades, HABs have occurred frequently in the East China Sea (ECS). Studies have shown that human activities contribute significantly to frequent HABs through eutrophication (Marcarelli et al. 2006; Shen et al. 2019a). The ECS is an optically complex Case-2 water body influenced by various factors, including freshwater input from the Yangtze River, the Taiwan Warm Current (TWC), and the Kuroshio Current, as well as regional climate change (Chen et al. 2006; Yang et al.

*Correspondence:
Chi Feng
fengchi@usts.edu.cn; fengchi9011@163.com
[1] School of Spatial Information and Mapping Engineering, Anhui University of Science and Technology, Huainan 232001, China
[2] School of Geographic Information and Tourism, Chuzhou University, Chuzhou 239000, China
[3] School of Geography Science and Geomatics Engineering, Suzhou University of Science and Technology, Suzhou 215009, China
[4] Key Laboratory of Marine Ecosystem Dynamics, Second Institute of Oceanography, Ministry of Natural Re-Sources, Hangzhou 310012, China
[5] Key Laboratory of Nearshore Engineering Environment and Ecological Security of Zhejiang Province, Hangzhou 310012, China
[6] State Key Laboratory of Satellite Ocean Environment Dynamics, Second Institute of Oceanography, Ministry of Natural Resources, Hangzhou 310012, China
[7] National Satellite Ocean Application Service, Ministry of Natural Resources of the People's Re-Public of China, Beijing 1000812, China

2020; Zeng et al. 2020). The coastal region of the ECS has sufficient condition for HABs with high concentrations of total suspended matter (TSM) and colored dissolved organic matter (CDOM) (Kiyomoto et al. 2001). The China Marine Disaster Bulletin reports that the number of HABs in the East China Sea has increased significantly since 2010. In 2021, the ECS experienced 26 algal blooms, with *Prorocentrumdonghaiense*(*P.donghaiense*) being the dominant species.

Ocean color satellite missions have contributed significantly to remote sensing by enabling HAB detection. Satellite imagery, characterized by wide coverage, daily visits, and low data latency, is considered a powerful HAB monitoring resource. Over several decades, multiple time-series ocean color satellite missions have been established, including the Sea-viewing Wide Field-of-view Sensor (SeaWiFS), Moderate Resolution Imaging Spectroradiometer (MODIS), and Visible Infrared Imaging Radiometer Suite (VIIRS) (Franz et al. 2012). Various methods have been developed for detecting blooms using satellite imagery, including anomalous chlorophyll a (Chl a)concentration, remote-sensing reflectance ($R_{rs}(\lambda)$) spectra, and the intrinsic optical properties of blooms. Shen et al. proposed the red tide detection index (RDI), which uses multi-source ocean color data to detect algal blooms in turbid coastal waters of the ECS (Shen et al. 2019b). Ahn et al. proposed a red tide index (RI) which combined the normalized water-leaving radiance of the SeaWiFS bands at 510, 555, and 443 nm for the detection of algal blooms in turbid waters (Ahn and Shanmugam 2006). Tao et al. combined *P.donghaiense* index (PDI) and the diatom index (DI) to successfully discriminate *P.donghaiense* from diatoms (Tao et al. 2015). Shang et al. employed the bloom index (BI), fluorescence line height (FLH), and total absorption coefficient at 443 nm (a (443)) as spectral indicators to differentiate between *dinoflagellate* and diatom blooms using MODIS data (Shang et al. 2014). Feng et al. proposed combining the spectral shape (SS) indices at 490nm (SS (490)) and 530nm (SS (530)) to detect blooms in the ECS based on GCOM-C data (Feng et al. 2023).

The Geostationary Ocean Color Imager (GOCI) is a remote sensor developed by the Korea Ocean Satellite Center to monitor marine ecological environments in Northeast Asia. GOCI was successfully launched onboard Communication, Ocean, and Meteorological Satellite (COMS) in 2010 as the first geostationary ocean remote-sensing satellite (Hoi et al. 2012). The original GOCI satellite had eight remote-sensing bands, including six visible-light bands (412, 443, 490, 660, and 680 nm) and two NIR bands (725 and 865 nm). The spatial resolution of the GOCI data reached 500 m. The first GOCI satellite was decommissioned in 2021 and followed by the GOCI-II, which was launched in February 2020. The spectral performance of GOCI-II improved as the number of visible bands increased from eight to thirteen, the spatial resolution is 250 m and ten images can be generated per day (Shin et al. 2021). In addition, the performance of satellite sensors changes after prolonged operation. For example, the MODIS-Aqua sensor has been in orbit for 21 years despite its intended lifespan of only 6 years. Therefore, its performance has started to decline (Meister et al. 2011). The specific parameters of the GOCI, GOCI-II and MODIS sensors are listed in Table 1. The efficiency of each bloom detection method varied for different sensors, as does the applicability in the same area. Currently, local validation of GOCI-II satellite data in the ECS is lacking.

Therefore, this study assessed the effectiveness of bloom detection for distinguishing various types of algal species using GOCI-II imagery. The three major objectives include verifying the validity of the GOCI-II satellite $R_{rs}(\lambda)$ data by matching it to the measured $R_{rs}(\lambda)$ data; comparing the feasibility of different bloom detection methods in the ECS using GOCI-II data; and finally, evaluating the effectiveness of GOCI-II data in distinguishing various bloom types, such as *P.donghaiense* and diatoms, as well as other blooms. These results provide useful information for applying GOCI-II data to ECS coastal observations.

Table 1 The specific parameters of GOCI, GOCI-II and MODIS

Parameters	GOCI/COMS	GOCI-II/COMS	MODIS/Aqua
Start date	June 2010	February 2020	May 2002
Horizontal resolution (m)	500	250	1000
Observational frequency	8 times/day	10 times/day	1 times/day
Central wavelength (nm)	412, 443, 490, 555, 660, 680, 745, 865	380, 412, 443, 490, 510, 555, 620, 660, 680, 709, 745, 865	412, 443, 469, 488, 531, 547, 555, 645, 667, 678
Bandwidth (nm)	8	12	10

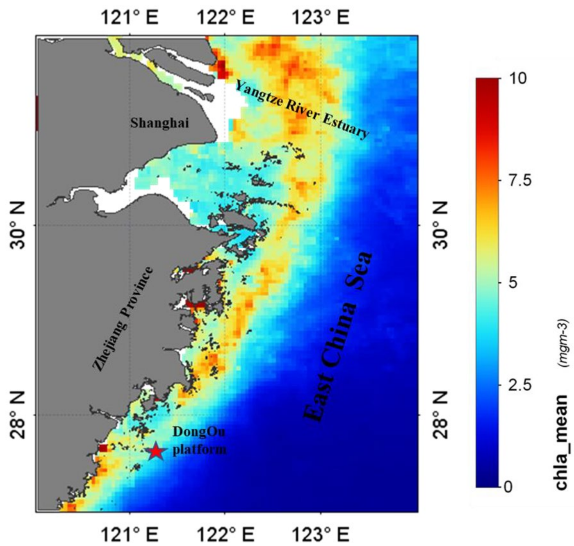

Fig. 1 The study area of the East China Sea (ECS). The red star represents the Dongou Ocean Observing Platform where in situ $R_{rs}(\lambda)$ observations were taken. The colored pixels represent Chlorophyll a (Chl a) concentrations from MODIS L3 1 km data obtained between 2011 and 2020

Data and methods

Study area and in situ measurements

The study area covered most of the ECS (26°N–33°N, 119°E–123°E), including the Yangtze River Estuary (YRE), Shanghai Municipality, and Zhejiang Province (Fig. 1).

Over the past decade, various factors have greatly influenced HABs in the ECS, such as monsoons, massive freshwater outflows, tides, and the Kuroshio current (Wang et al. 2007). The 2021 HAB records for the ECS were collected from the State Oceanic Administration of China and the China Marine Disaster Bulletin. These data included detailed information on the time, location, spatial range, and pathogenic species involved in the HABs (see Table 2). Based on the records of algal species, various methods for detecting HABs are summarized in Table 3.

The fixed Dongou ocean observation platform (27.675°N, 121.355°E) was used to collect $R_{rs}(\lambda)$ data and normalized water-leaving radiance (L_{wn}) data in the ECS from January to September 2021 (Fig. 1). The observation platforms were equipped with a Sea-Viewing Wide Field-of-View Sensor (SeaWiFS) Photometer Revision for Incident Surface Measurements (SeaPRISM) autonomous radiometer system. Measurements were taken every 30 min from 8:00 am to 16:00 pm. The system collected and processed water surface and sky radiation data to obtain L_{wn} data, then divided these values by the average extraterrestrial solar radiation (F_0) of the corresponding band to obtain the $R_{rs}(\lambda)$ data (Schmutz et al. 2013). The SeaPRISM system was configured to measure ocean color at 11 wavelengths ranging from 400 to 1020 nm. The data were manually examined to ensure spectral data accuracy. This study used the $R_{rs}(\lambda)$ data obtained from the central bands at 412, 443, 490, 510, 555, 620, 660, and 865 nm for matching analysis and comparison to GOCI-II data.

Satellite data

The GOCI-II satellite was launched in February 2020 and the standard GOCI-II Level-2 data were obtained from the Korea Ocean Color Satellite Center (https://www.nosc.go.kr/eng/main.do). The MODIS-Aqua data for the corresponding period were obtained from the NASA ocean color website (http://oceancolor.gsfc.nasa.gov/).

During the Universal Time Coordinated (UTC) period from 3:00 to 5:00, the ECS region was mostly cloud-free. The GOCI-II satellite data were validated using GOCI-II Level-2 data from January to September 2021. In addition, four bloom detection methods were evaluated using GOCI-II imagery on June 7, September 1, and September 21, 2021. The classification of various algal species was evaluated based on GOCI-II data obtained on September 1 and September 21, 2021.

Table 2 East China Sea algal bloom events in 2021

Date	Center location	Data usage	Species	Algal bloom location
6.3–6.10	121.092°E, 27.491°N	Bloom detection	*Prorocentrumdonghaiense* (*P.donghaiense*)	Wenzhou coasts
9.1–9.8	121.515°E, 28.546°N	Bloom detection	*Chaetoceroscurvisetus* (*C.curvisetus*)	Taizhou coasts
9.19–10.6	121.216°E, 28.152°N	Bloom detection	*Akashiwosanguinea* (*A.sanguinea*)	Taizhou and Wenling coasts
9.1	121.468°E, 28.763°N	Harmful algae discrimination	*C.curvisetus*	Taizhou coasts
9.21	121.381°E, 28.475°N	Harmful algae discrimination	*A.sanguinea*	Yuhuan coasts

Table 3 Four algorithms for detecting harmful algal blooms

Algorithm	MODIS	GOCI-II	Threshold value	References
$\mathrm{RI}=\frac{R_{rs}(\lambda^{+})-R_{rs}(\lambda^{-})}{R_{rs}(\lambda)-R_{rs}(\lambda^{-})}$	$\lambda^{+}=555$ $\lambda^{-}=443$ $\lambda=488$	$\lambda^{+}=555$ $\lambda^{-}=443$ $\lambda=490$	RI > 2.8	Lou and Hu (2014)
$\mathrm{SS}(\lambda)=R_{rs}(\lambda)-R_{rs}(\lambda^{-})-(R_{rs}(\lambda^{+})-R_{rs}(\lambda^{-}))\times\frac{\lambda-\lambda^{-}}{\lambda^{+}-\lambda^{-}}$	$\lambda^{+}=555$ $\lambda^{-}=488$ $\lambda=531$	$\lambda^{+}=555$ $\lambda^{-}=490$ $\lambda=510$	SS (510) < 0	Wynne et al. (2008)
$\mathrm{LHR}=\frac{\mathrm{LH}(\lambda_1)}{\mathrm{LH}(\lambda_2)}$ $\mathrm{LH}(\lambda_i)=R_{rs}(\lambda_i)-R_{rs}(660)-(R_{rs}(745)-R_{rs}(660))\times\frac{(\lambda_i-660)}{(745-660)}$	*1	$\lambda_1=709$ $\lambda_2=680$	LHR > 0.6	Tao et al. (2011)
$R_{AB}=\frac{R_{rs}(\lambda^{+})}{R_{rs}(\lambda^{-})}$	λ^{+}=555 λ^{-}=531	$\lambda^{+}=555$ $\lambda^{-}=510$	$R_{AB}>1.25$	Tao et al. (2015)

*1 LHR method is developed for MERIS satellite (λ_1=709, λ_2=681)

Data processing

Data preprocessing was necessary to ensure high-quality satellite images because of sensor characteristics, atmospheric conditions, and external interference. SeaDAS7.5.3 software was used for geometric correction, reprojection, and image clipping of standard GOCI-II Level-2 data (Ocean Biology Processing Group (OBPG), http://oceancolor.gsfc.nasa.gov/).

Furthermore, match-up comparison analyses were performed using linear regression between the in situ and satellite data. Initially, 108 data points were collected from the Dongou observation platform near the coast. However, only 64 useable points were obtained because the GOCI-II satellite was affected by nearshore atmospheric correction due to the proximity of the mainland. Nearest neighbor pixels were selected to match the local $R_{rs}(\lambda)$ data using 3×3 pixel windows. Effective pixels around the target position that were unable to reach a 3×3 pixel window were considered invalid and discarded. Finally, 64 pairs of satellite and in situ $R_{rs}(\lambda)$ data were matched for accuracy evaluation.

The statistical parameters used included the average absolute percentage difference (APD), root mean square error (RMSE), bias, and coefficient of determination (R^2):

$$\mathrm{APD}=\frac{1}{N}\sum_{i=1}^{N}\left|\frac{Y_i-X_i}{X_i}\right|\times 100, \tag{1}$$

$$\mathrm{RMSE}=\sqrt{\frac{1}{N}\sum_{i=1}^{N}(Y_i-X_i)^2}, \tag{2}$$

$$\mathrm{Bias}=\frac{1}{N}\sum_{i=1}^{N}(Y_i-X_i), \tag{3}$$

where X_i is the in situ observation value, Y_i is the satellite data, and N is the number of matches between the in situ and GOC-II data. The coefficient of determination was calculated for each wavelength to provide better data matching information.

HABs detection methods

The band ratio and spectral shape difference methods are widely used for extracting bloom information. This study used the red tide index (RI) (Lou and Hu 2014), spectral shape (SS) (Wynne et al. 2008), red band line height ratio (LHR) (Tao et al. 2011), and algal bloom ratio (R_{AB}) (Tao et al. 2015) to compare bloom detection methods. For detailed information about each of these methods, refer to Table 3.

To classify various algal species, three methods were selected in this study (Table 4): the bloom index (BI) (Shang et al. 2014), spectral slope ($R_{\_slope}$) (Shen et al. 2019b), and the combined *P.donghaiense* index (PDI) and diatom index (DI) (Tao et al. 2015). Because these algorithms were originally developed for the MODIS and MERIS satellites, band adjustments were necessary when using the GOCI-II satellite to extract blooms data. The specific details of these adjustments are presented in Tables 3 and 4.

Result

Validation of GOCI-II $R_{rs}(\lambda)$

The accuracy of remote-sensing methods for algal bloom monitoring depends on the quantification level of satellite-derived $R_{rs}(\lambda)$. Figure 2 shows the results of matching analysis between GOCI-II and in situ $R_{rs}(\lambda)$ data. The GOCI-II $R_{rs}(\lambda)$ was overestimated at short wavelengths at 412 and 443 nm when $R_{rs}(\lambda) > 0.01sr^{-1}$.

The GOCI-II data exhibited strong correlations with the in situ data at wavelengths of 490, 510, 620, and 660

Table 4 Three algorithms for differentiation of *P.donghaiense* and diatom blooms

Algorithm	MODIS	GOCI-II	Threshold value	References
$BI = \frac{(R_{rs}(\lambda_1)-R_{rs}(\lambda_2))/(\lambda_1-\lambda_2)}{(R_{rs}(\lambda_3)-R_{rs}(\lambda_4))/(\lambda_3-\lambda_4)}$	$\lambda_1 = 488$, $\lambda_2 = 443$ $\lambda_3 = 555$, $\lambda_4 = 531$	$\lambda_1 = 490$, $\lambda_2 = 443$ $\lambda_3 = 555$, $\lambda_4 = 510$	If $0 < BI \leq 0.3$, *P.donghaiense*; If $0.3 < BI \leq 1.0$, diatom	Shang et al. (2014)
$PDI = \frac{R_{rs\_slope}(\lambda,\lambda^+)-R_{rs\_slope}(\lambda^+,\lambda^-)}{R_{rs}(\lambda)-R_{rs}(\lambda^-)}$ *2 $DI = \frac{R_{rs}(\lambda_1)-[R_{rs}(\lambda)+\frac{(\lambda-\lambda_1)}{(\lambda-\lambda_2)}\times(R_{rs}(\lambda_2)-R_{rs}(\lambda))]}{R_{rs}(\lambda_1)}$	$\lambda^+ = 531$, $\lambda^- = 488$ $\lambda = 555$, $\lambda_1 = 645$, $\lambda_2 = 667$	$\lambda^+ = 510$, $\lambda^- = 490$ $\lambda = 555$, $\lambda_1 = 620$ $\lambda_2 = 660$	If $DI < 25 \times PDI - 0.125$, *P.donghaiense*; If $DI \geq 25 \times PDI - 0.125$, diatom	Tao et al. (2015)
$R_{\_slope} = \tan^{-1}(100 \times (1 - (R_{rs}(\lambda_2) - R_{rs}(\lambda_1))/(\lambda_2 - \lambda_1)$	$\lambda_1 = 667$, $\lambda_2 = 555$	$\lambda_1 = 660$, $\lambda_2 = 555$	if $R_{\_slope} > 0.4$, *P.donghaiense;* if $R_{\_slope} < 0.4$, *diatom*	Shen et al. (2019b)

$^{*}2 R_{rs\_slope}(\lambda, \lambda^+) = (R_{rs}(\lambda) - R_{rs}(\lambda^+))/(\lambda - \lambda^+)$

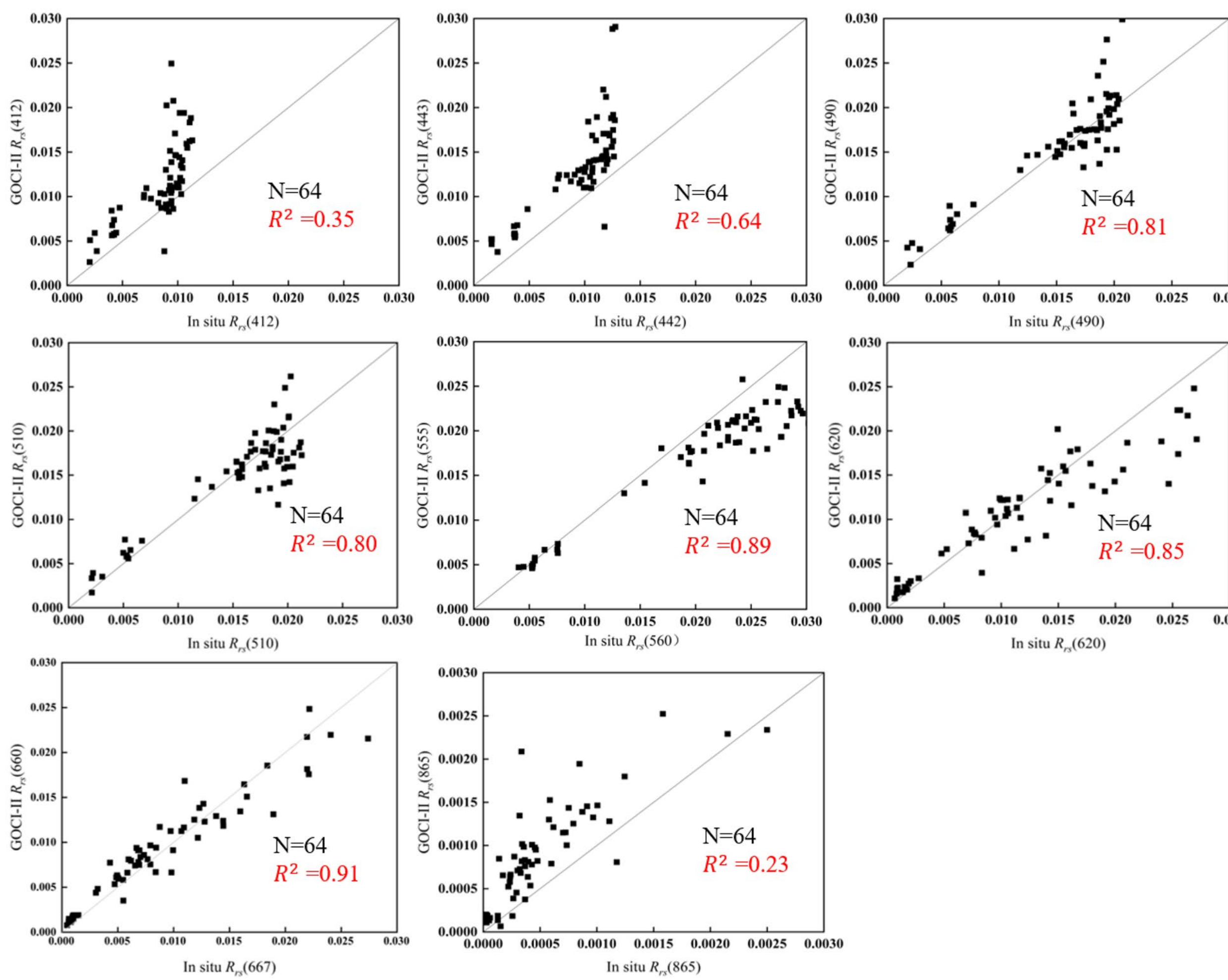

Fig. 2 Scatterplots showing the correspondence between in situ $R_{rs}(\lambda)$ and GOCI-II satellite remote sensing ($R_{rs}(\lambda)$; sr^{-1}) data at 412, 443, 490, 510, 555, 620, 660, and 865 nm

Table 5 Statistical comparison of in situ and GOCI-II $R_{rs}(\lambda)$ data

Parameters bands (nm)	R^2	RMSE	APD	Bias
412	0.35	0.006	50.07%	0.0038
443	0.64	0.005	50.40%	0.0038
490	0.81	0.002	14.73%	0.0005
510	0.80	0.002	14.29%	− 0.0004
555	0.89	0.004	14.65%	− 0.0033
620	0.85	0.003	29.36%	− 0.0008
660	0.91	0.002	28.98%	0.0003
865	0.23	0.003	158.92%	0.0007

nm when $R_{rs}(\lambda) < 0.02sr^{-1}$. However, the GOCI-II data significantly underestimated the values at 555, 620, and 660 nm when $R_{rs}(\lambda) > 0.02sr^{-1}$, while total overestimation was also observed, specifically at 865 nm.

The R^2, RMSE, APD and bias for the in situ and GOCI-II data are displayed in Table 5. The R^2 values at 412, 443 and 865 nm were 0.35, 0.64, and 0.23, respectively. However, the R^2 values at 490, 510, 620 and 660 nm were greater than 0.8, indicating a significant dependence on the spectral characteristics. The APD values at each band were 50.07% (412 nm), 50.40% (443 nm), 14.73% (490 nm), 14.29% (510 nm), 14.65% (555 nm), 29.36% (620 nm), and 28.98% (660 nm). The RMSE value peaked at 0.006 at 412 nm.

In summary, these results indicated a high level of spectral consistency between the GOCI-II and in situ data, particularly at wavelengths of 490, 510 and 555 nm. However, high uncertainties were observed at 412 and 443 nm.

HABs detection using GOCI-II data

Figure 3 depicts the spectral curves of satellite-averaged $R_{rs}(\lambda)$ values of bloom, turbid, and clear water obtained from June to September 2021. The peak reflectance of clean water was mainly visible in the blue light band, and the spectral reflectance showed a decreasing trend. Turbid water exhibited absorption characteristics in the short bands at 443 and 490 nm, with reflection peaks at 555 nm. Moreover, turbid water distinguishable from bloom water when $R_{rs}(\lambda) > 0.014sr^{-1}$.

The three algae species showed similar spectral characteristics (Fig. 3a). First, prominent absorption properties were exhibited in the short bands at 443 and 490 nm. The reflection peaks reached their maxima at 555 nm, while the reflection values were relatively low at 510 nm. Finally, a smaller reflection shoulder was observed in the near-infrared bands between 675 and 700 nm. As the wavelength increased beyond 555 nm, the reflectivity gradually decreased and remained stable between 750 and 865 nm. In comparison, MODIS has limited wavelength range spectral curves and could not effectively demonstrate these features.

Figure 4a–d shows examples of the detection methods for *P.donghaiense*. The LHR method did not extract blooms on the coast of Wenzhou (Fig. 4c), which was inconsistent with the reported bloom events during the summer of 2021. In comparison, the other three methods exhibited superior extraction performance. In the region between 29°N and 30°N, a small range of HABs events was observed (Fig. 4b). Figure 4e–h shows examples of detection methods for *C.curvisetus*. As shown in Fig. 4e, f and h, large-scale HABs were identified in the Zhejiang coastal area, especially using SS (510)

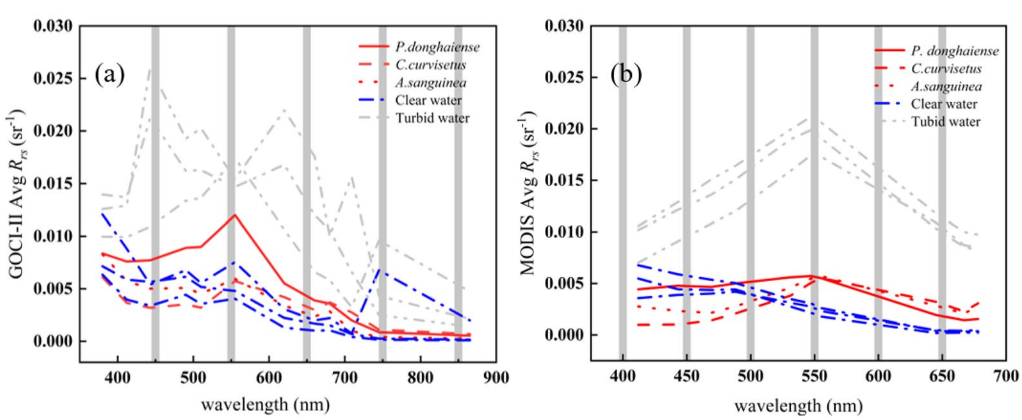

Fig. 3 The average $R_{rs}(\lambda)$ spectral curves of **a** GOCI-II and **b** MODIS data. The gray columns indicated the wavelengths of GOCI-II and MODIS satellites. (*P.donghaiense*, *C.curvisetus*, and*A.sanguinea* occurred on June 7, September 1 and September 21, 2021, respectively)

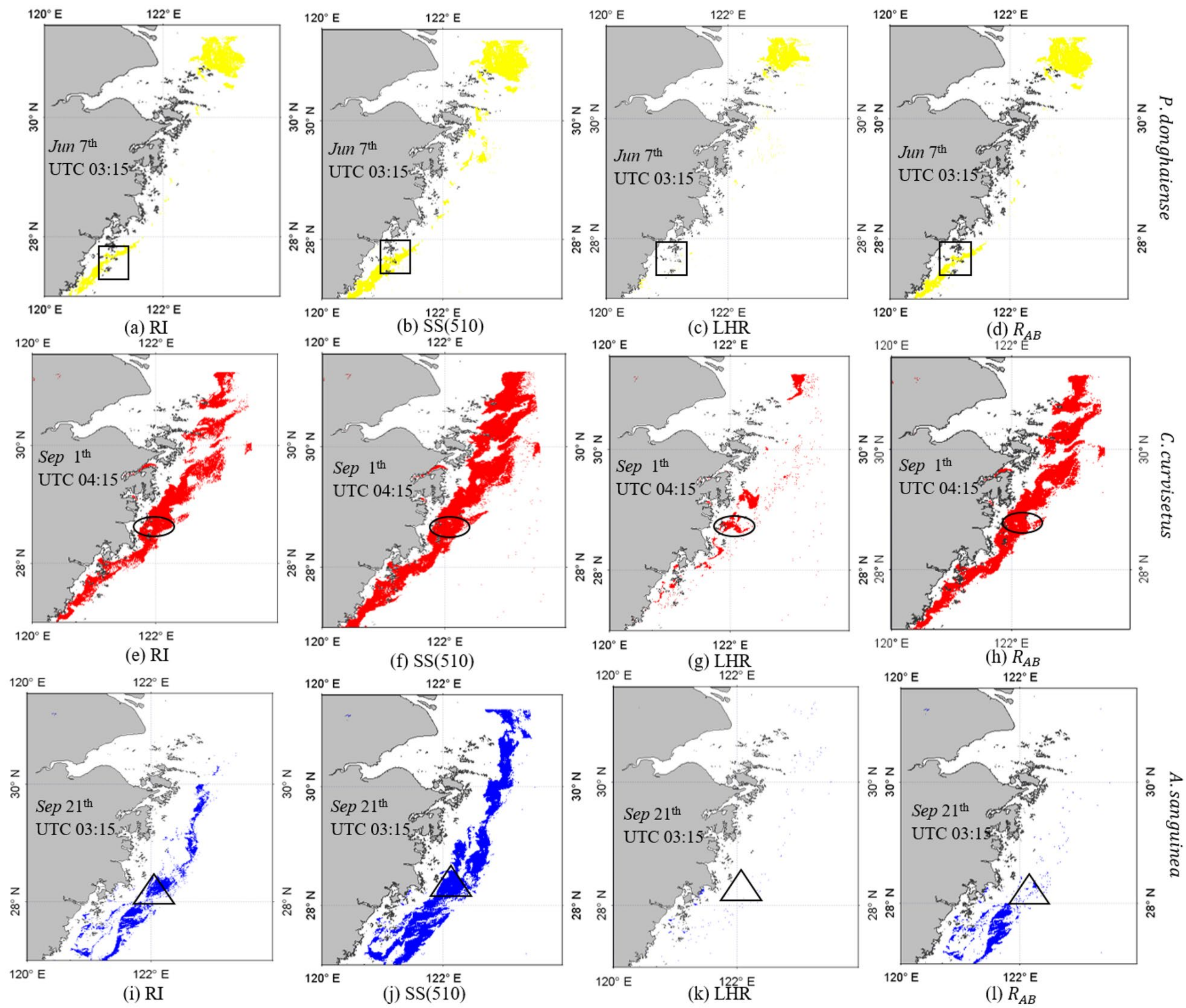

Fig. 4 Bloom detection results (**a**–**d**) *P.donghaiense*, (**e**–**h**) *C.curvisetus*, and (**i**–**l**) *A.sanguinea* using four methods: RI > 2.8, SS(510) < 0, LHR > 0.6, and $R_{AB} > 1.25$ from GOCI-II imagery on June 7, September 1 and September 21, 2021, respectively. Black rectangles, circles, and triangles represent the *P.donghaiense*, *C.curvisetus*, and *A.sanguinea* blooms, respectively

imagery. This indicated that the RI, SS (510), and R_{AB} methods were suitable for monitoring diatom blooms. However, in the coastal areas of the ECS, effectively extracting HABs using LHR > 0.6 was difficult. From Fig. 4i–l, the SS (510) method exhibited the best extraction efficiency for detecting *A.sanguinea*, followed by the RI method. As shown in Fig. 4k, the LHR method yielded a negative result in the coastal areas of Taizhou where *A.sanguinea* blooms were not observed. Despite successfully capturing large-scale HABs in the southern areas of Taizhou using $R_{AB} > 1.25$, the SS (510) method was superior with the best bloom detection capability. This was followed by the RI and R_{AB} methods, whereas the LHR method was not satisfactory.

Distinguishing of diatom and dinoflagellate blooms using GOCI-II data

Based on the bloom detection results for September 1, and September 21, 2021, the BI (Shang et al. 2014), spectral shape ($R_{\_slope}$) (Shen et al. 2019b), and combined PDI and DI (Tao et al. 2015) methods were used for the discrimination of algal species.

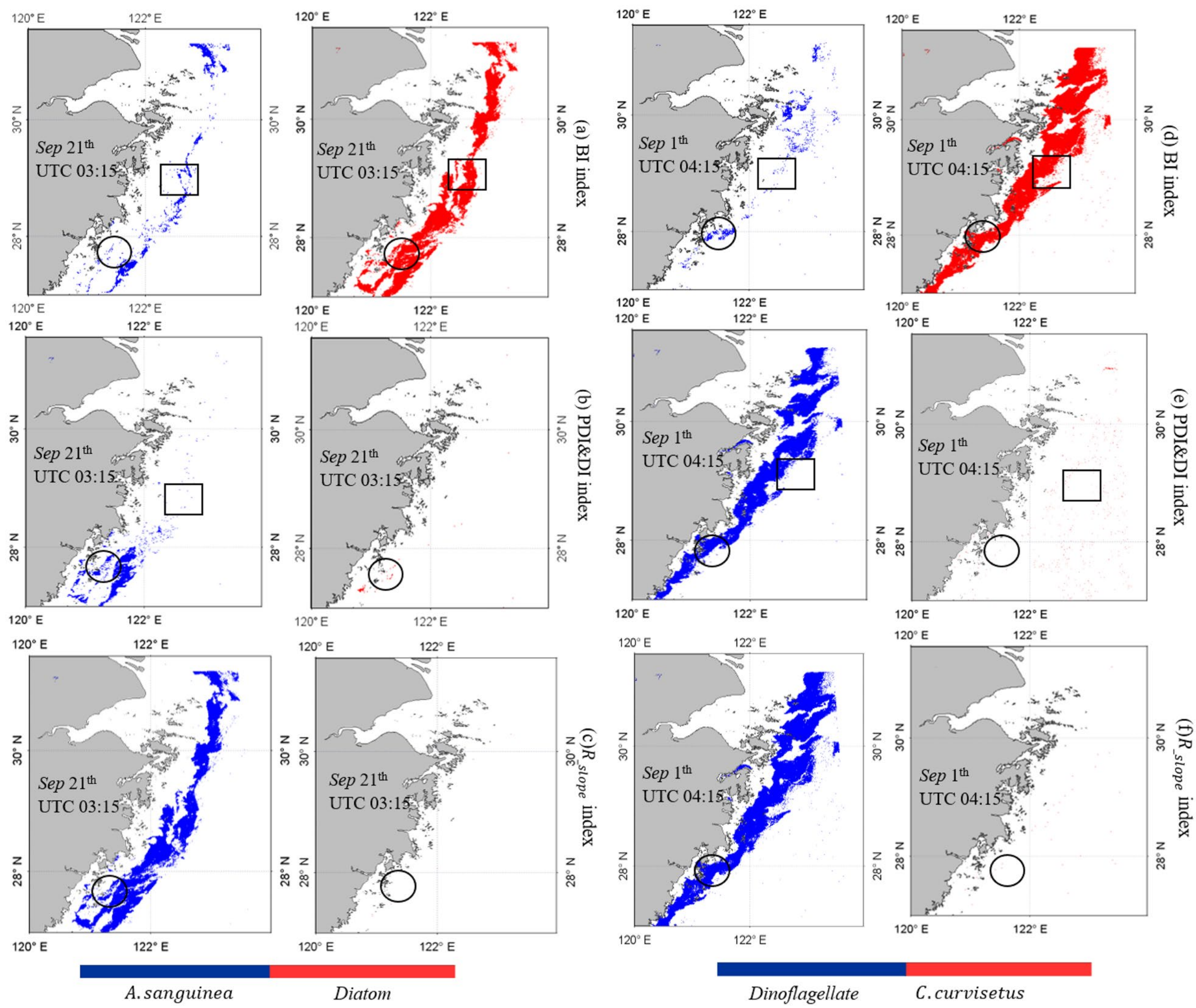

Fig. 5 Results of bloom type classification derived from existing models from September 1 and September 21, 2021 separately. **a** BI index (Shang et al. 2014), **b** PDI and DI index (Tao et al. 2015), and **c** $R_{\_slope}$ index (Shen et al. 2019b). The squares and circles represent the sea areas south of Taizhou and Yuhuan as the centers, respectively

There were distinct differences in the classification results of algal species using different methods on GOCI-II imagery captured on the same day. Among them, BI was superior to the combined PDI and DI, whereas the $R_{\_slope}$ method performed the worst, as shown in Fig. 5. To evaluate the three algorithms, a comparative analysis was conducted on local regions (the square and circles in Fig. 5). In the ECS, the dominant species alternate between *A.sanguinea* (Fig. 5a–c), and *C.curvisetus* (Fig. 5d–f). These observations are consistent with the findings reported in the 2021 China Marine Disaster Bulletin. According to Shang et al. (Shang et al. 2014), the BI threshold derived from MODIS was lower than 0.3. This threshold value provided a reliable assessment for classifying between dinoflagellates and diatoms on the Xiangshan and Yuhuan coasts (Fig. 5a and d). However, the spatial distribution of algal blooms in coastal areas south of Taizhou (Fig. 5b, c, e, and f) suggested that using GOCI-II data is inadequate for identifying HABs. No algal blooms were detected in the coastal area of the Yangtze Estuary (Fig. 5b), whereas numerous algal blooms were found in this region, as shown in Fig. 5a and c. Moreover, the combined PDI and DI algorithm could only distinguish between diatoms and dinoflagellates in the coastal region of Yuhuan (Fig. 5b and e). The $R_{\_slope}$ method failed to distinguish between diatoms and dinoflagellates in the ECS. The performances of the combined PDI and DI, and $R_{\_slope}$ method using MODIS

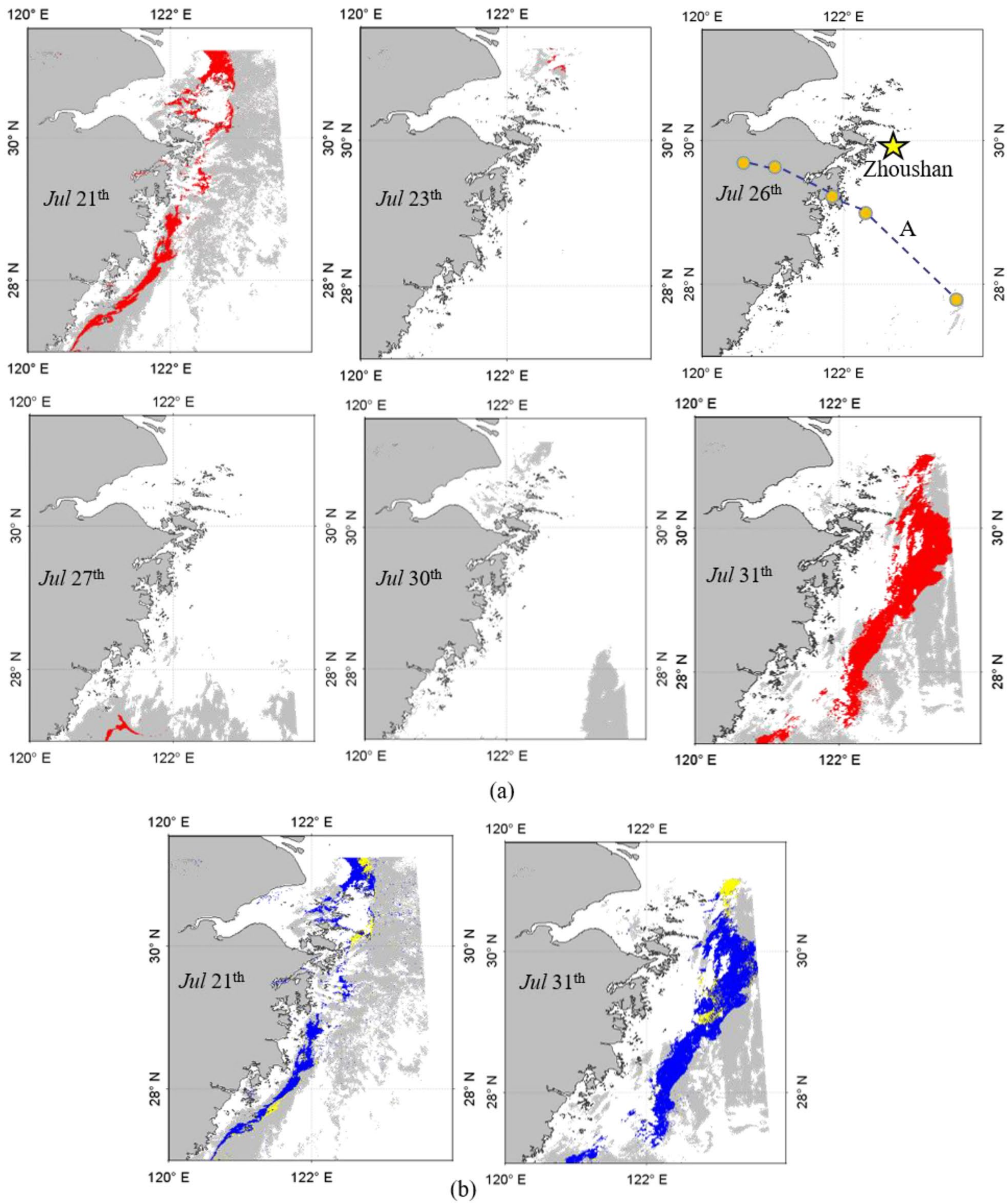

Fig. 6 **a** Distribution of bloom detection area using the SS (510) method during the landfall period of Typhoon Yanhua using GOCI-II data from July 21 to July 31, 2021. Red indicates the bloom area extracted by SS (510) and grey indicates the non-bloom area. **b** Discrimination of algal species using the BI method before and after Typhoon Yanhua landed by GOCI-II data on July 21 and July 31, 2021, respectively. Yellow indicates dinoflagellate bloom waters and blue indicates diatom bloom waters. The yellow star represents the landfall of Typhoon Yanhua in Zhoushan, Zhejiang Province, on July 25, 2021. Region A represents the trajectory of Typhoon Yanhua landing in the ECS area from July 24 to July 27, 2021

were satisfactory; however, they may not be suitable for GOCI-II.

Monitoring bloom variations using GOCI-II data

The effects of the typhoons on algal blooms were examined to assess the potential of GOCI-II data for monitoring algal blooms under climate-change conditions. According to the 2021 National Hydrological Annual Report (China), a strong typhoon named Yanhua reached China's coast from July 25 to July 28, 2021. A series of GOCI-II data was analyzed to characterize the spatial range of blooms before and after the typhoon event (Fig. 6).

Before the typhoon landed on July 21, 2021, the spatial distribution of algal blooms across the ECS was uneven (Fig. 6a). A small patch of bloom water was observed in the Yangtze River Estuary. Slim bloom patches were also found along the coast of Zhejiang Province. During the landing periods on July 25 and July 26, limited valid pixels were observed near the coast owing to cloud coverage. The red tide area increased significantly after the typhoon passed on July 31, 2021. Specifically, the bloom area increased offshore of the Zhejiang Province coast. Minor blooms were observed near the shore. The BI method was applied to study the changes in algal species before and after the typhoon (Fig. 6b). Both dinoflagellate and diatom bloom waters were observed along the coast of Zhejiang Province. Specifically, there were relatively more dinoflagellate blooms before the typhoon struck, whereas there was a marked increase in both diatoms and dinoflagellates after the typhoons. The use of GOCI-II data to analyze algae species and distribution before and after typhoon Yanhua provides a foundation for future research into the effects of typhoons on the ecological environment of ECS.

Discussion

A match-up analysis between satellite and in situ $R_{rs}(\lambda)$ data was conducted (Fig. 2). The satellite-derived $R_{rs}(\lambda)$ at bands of 412, 443, and 865 nm had larger values than those obtained through local measurements. This was potentially due to large amounts of the suspended particulate matter (SPM) in the Yangtze River Estuary. Abundant SPM in water may result in higher $R_{rs}(\lambda)$ in the visible and near-red bands (Wang, et al. 2020). Moreover, the overestimation of the satellite-derived $R_{rs}(\lambda)$ may result from the uncertainties in atmospheric correction. The interactions between water vapor and aerosol at bands of 620, 660, and 865 nm may impact satellite $R_{rs}(\lambda)$ retrieval accuracy (Lee et al. 2023). The local $R_{rs}(\lambda)$ measurement was obtained in the southern region of Zhejiang Province, and additional GOCI data capturing was planned despite abundant preexisting in situ data.

Various bloom detection methods were compared using GOCI-II imagery. The SS (510) method was more appropriate for extracting blooms than the RI,R_{AB} and LHR methods (Fig. 4). The limitations of the RI approach included only considering the height difference between satellites $R_{rs}(\lambda)$ in the blue and green bands and not the change in spectral curves within this range. Figure 7a illustrates the area of bloom water extracted by RI > 2.8 method and the area of turbid water extracted using the threshold of $R_{rs}(555) > 0.014sr^{-1}$. The area between the

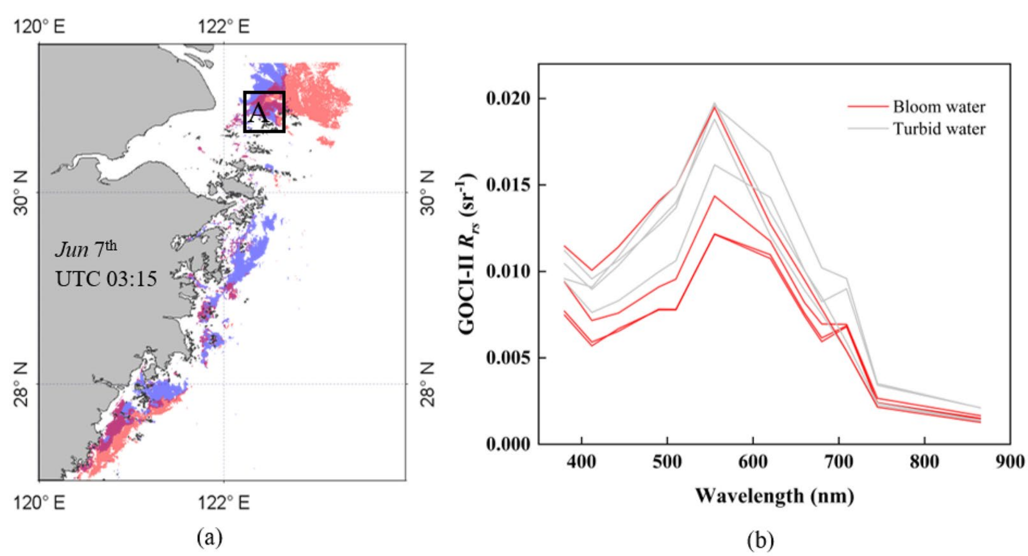

Fig. 7 **a** Bloom detection results using the RI method and GOCI-II data on June 7, 2021. The red area indicates bloom water; the blue area indicates turbid water; and the region A indicates the overlap of bloom and turbid water. Note that the turbid pixels were assessed using $R_{rs}(555) > 0.014sr^{-1}$. **b** Samples of R_{rs} spectral curves from turbid water and bloom water in region A

bloom and turbid waters in the Yangtze River Estuary overlapped (Region A in region 7a). Given the complex optical properties of turbid waters, such regions may be falsely identified as bloom water because of the complex constituents of algal and non-algal particles. The $R_{rs}(\lambda)$ spectrun of turbid water closely resembled the ones from bloom waters (Fig. 7b). Therefore, the combination of RI > 2.8 and $R_{rs}(555) < 0.014sr^{-1}$ improved bloom extraction accuracy significantly. The R_{AB} method proposed by Tao et al. was developed to detect blooms using MODIS satellite (Tao et al. 2015). However, the extraction results from GOCI-II imagery of bloom water were unreliable due to the absence of a band near 531 nm and the strong absorption of $R_{rs}(\lambda)$ at 510 nm. The non-algal substances in bloom waters reduce chlorophyll fluorescence signals in coastal waters (McKee et al. 2007), which affect bloom extraction using the LHR method.

In the final step, three classification methods were employed to identify dinoflagellate and diatom blooms using GOCI-II imagery, as illustrated in Fig. 5. The BI method was superior to the combined PDI and DI as well as the $R_{\_slope}$ method for classifying phytoplankton groups. Therefore, caution should be exercised when using these approaches. The PDI and DI methods were originally proposed based on the MODIS satellite imagery, while the GOCI-II satellite imagery used the 510 nm band instead of the 531 nm band. This may affect the accuracy of the method in the ECS. The $R_{rs}(\lambda)$ errors at 510, 620, and 660 nm may cause differences in algae species discrimination. Another important potential factor is the uncertainty of the atmospheric correction in coastal areas.

Conclusion

This study used GOCI-II data to detect HABs methods in the ECS and evaluate methods for distinguishing different algal species. Initially, the accuracy of GOCI-II $R_{rs}(\lambda)$ was verified by matching GOCI-II satellite data with in situ data. The bands at 412 and 443 nm exhibited high inaccuracy and overestimation in the near-infrared band, whereas the data quality was improved at 490, 510, and 620 nm. Second, the applicability of the different HABs methods to the ECS varied. After conducting a comprehensive comparative analysis of four existing HABs extraction methods, namely SS (510), RI, R_{AB}, and LHR, the SS (510) method yielded the best results compared to RI. However, both R_{AB} and LHR showed poor results because they used a substitute band at 510 nm. The adoption of BI, $R_{\_slope}$ and combined PDI and DI methods was crucial for distinguishing between different algal species. Although the BI method was effective for differentiation, the combined PDI and DI method as well as the $R_{\_slope}$ method were not helpful in distinguishing dinoflagellates and diatoms. Further field and satellite observations are required to improve existing methods HABs monitoring methods. Additional modifications are necessary to enhance the accuracy of HABs monitoring methods and differentiate between types of algal blooms.

Beyond the preliminary examination of the GOCI-II images, this study further delves into the aftermath of Typhoon "Yanhua" on the blooms in the ECS. The findings suggest that the area and scope of the algal blooms notably augmented post-passage of the typhoon. This is vital for further ECS research and improving marine ecosystem management However, the occurrence of algal blooms is not solely reliant on the typhoon, but also interrelated to multiple factors such as sea water temperature and salinity. These elements may have complex interactions. Thus, future research and exploration are imperative.

Acknowledgements
The author thanks KOSC for providing GOCI-II data, and NASA for providing MODIS data. Sincere thanks for Qingjun Song, Bangyi Tao, Changpeng Li and Yuanli Zhu for providing local observations of $R_{rs}(\lambda)$ from the Dongou ocean observation platform. The author also expresses gratitude to the team members who made significant contributions to the data collection and measurement in the field and laboratory. Finally, the authors greatly appreciate the constructive opinions and suggestions of the editors and potential reviewers.

Author contributions
Conceptualization, YJ and CF; methodology, YJ and CF; validation, YJ and CF; investigation, TC, YZ, CL, BT and QS; writing—original draft preparation, YJ, CF and TC; writing—review and editing, YJ and CF; data availability, YZ, CL, BT and QS. All authors have read and agreed to the published version of the manuscript.

Funding
This work was supported by the National Natural Science Foundation of China under Grants [42271443], the Anhui Provincial Natural Science Foundation [2208085Y15] and Top Scholar of Anhui Provincial Department of Education [gxbjZD2021079].

Availability of data and materials
The datasets used during the current study are available on reasonable request from the corresponding author.

Declarations

Competing interests
The authors declare that they have no competing economic interests or personal relationships.

Received: 13 June 2023 Accepted: 13 December 2023
Published online: 18 January 2024

References

Ahn Y, Shanmugam P (2006) Detecting the red tide algal blooms from satellite ocean color observations in optically complex Northeast-Asia Coastal waters, Remote Sens. Environ 103:419–437
Chen HL, Lu SH, Zhang CS, Zhu DD (2006) A survey on the red tide of Prorocentrum donghaiense in East China Sea, 2004. Ecol Sci 25(3):226–230
Feng C, Zhu Y, Shen A, Li C, Song Q, Tao B, Zeng J (2023) Assessment of GCOM-C satellite imagery in bloom detection: a case study in the East China Sea. Remote Sens 15:691
Franz B A, Bailey S W, Meister G, Werdell P J. (2012). Quality and consistency of the NASA ocean color data record. In: Proceedings of the Ocean Optics XXI, Glasgow, UK
Hallegraeff GM, Anderson DM, Cembella AD (2003) Manual on harmful marine microalgae. UNESCO, Paris
Hoi J-K, Park YJ, Ahn JH, Lim H-S, Eom J, Ryu J-H, Choi C, Park YJ, Ahn JH, Lim H-S et al (2012) GOCI, the world's first geostationary ocean color observation satellite, for the monitoring of temporal variability in coastal water turbidity. J Geophys Res Ocean 117:9004
Kiyomoto Y, Iseki K, Okamura K (2001) Ocean color satellite imagery and shipboard measurements of chlorophyll a and suspended particulate matter distribution in the East China Sea. J Oceanogr 57:37–45
Lee K-S, Park M-S, Choi J-K, Ahn J-H (2023) Improvement of GOCI-II water vapor absorption correction through fusion with GK-2A/AMI data. Remote Sens 15:2124
Lou X, Hu C (2014) Diurnal variation harmful algal blooms in the East China Sea observations from GOCI. Remote Sens Environ 140:562–572
Lu D, Goebel J, Qi Y, Zou J, Han X, Gao Y et al (2005) Morphological and genetic study of Prorocentrum donghaiense Lu from the East China Sea, and comparison with some related Prorocentrum species. Harmful Algae 4:493–505
Marcarelli AM, Wurtsbaugh WA, Griset O (2006) Salinity controls phytoplankton response to nutrient enrichment in the great Salt Lake, Utah USA. Can J Fish Aquat Sci 63:2236–2248
McKee D, Cunningham A, Wright D, Hay L (2007) Potential impacts of non-algal materials on water leaving Sun induced chlorophyll fluorescence signals in coastal waters. Appl Opt 46:7720–7729
Meister G, Franz BA, Kwiatkowska EJ et al (2011) Corrections to the calibration of MODIS Aqua ocean color bands derived from SeaWiFS data. IEEE Trans Geosci Remote Sens 50(1):310–319
Schmutz W, Fehlmann A, Finsterle W, Kopp G, Thuillier G (2013) Total solar irradiance measurements with Premos/picard. AIP Conf Proc 1531:624–627
Shang S, Wu J, Huang B, Lin G, Lee Z, Liu J, Shang S (2014) A new approach to discriminate dinoflagellate from diatom blooms from space in the East China Sea. J Geophys Res Oceans 119:4653–4668. https://doi.org/10.1002/2014JC009876
Shen F, Tang R, Sun X, Liu D (2019a) Simple methods for satellite identification of algal blooms and species using 10-year time series data from the East China Sea. Remote Sens Environ 235:111484
Shen F, Tang R, Sun X, Liu D (2019b) Simple methods for satellite identification of algal blooms and species using 10-year time series data from the East China Sea. Remote Sens Environ 235:111484
Shin J, Lee J-S, Jang L-H, Lim J, Khim B-K, Jo Y-H (2021) Sargassum detection using machine learning models: a case study with the first 6 months of GOCI-II imagery. Remote Sens 13:4844
Tang D, Di B, Wei G, Ni IH, Oh IS, Wang S (2006) Spatial, seasonal and species variations of harmful algal blooms in the South Yellow Sea and East China Sea. Hydrobiologia 568:245–253
Tao B, Mao Z, Wang D, Lu J, Huang H (2011) The use of MERIS fluorescence bands for red tides monitoring in the East China Sea. In: Remote sensing of the ocean, sea ice, coastal waters, and large water regions, 81751K. SPIE, Prague
Tao B, Mao Z, Lei H, Pan D, Shen Y, Bai Y, Zhu Q, Li Z (2015) A novel method for discriminating Prorocentrum donghaiense from diatom blooms in the East China Sea using MODIS measurements. Remote Sens Environ 158:267–280
Wang Z, Li L, Chen D, Xu K, Wei T, Gao J, Zhao Y, Chen Z, Masabate W (2007) Plume front and suspended sediment dispersal off the Yangtze (Changjiang) River mouth, China during non-flood season. Estuar Coast Shelf Sci 71:60–67
Wang S et al (2020) Remote sensing of water turbidity in the eastern China seas from geostationary ocean color imager. Int J Remote Sens 41(11):4080–4101
Wynne TT, Stumpf RP, Tomlinson MC, Warner RA, Tester PA, Dyble J, Fahnenstiel GL (2008) Relating spectral shape to cyanobacterial blooms in the Laurentian Great Lakes. Int J Remote Sens 29:3665–3672
Yang Y, Liu PX, Zhou HH, Xia LH (2020) Evaluation of the change trend and health status of marine organisms in the Changjiang estuary in the past 15 years. J Ecol 40:8892–8904
Zeng Y, Lu D, Wang P, Guo R, Guan W, Dai X (2020) Further study on the relationship between the protochlorophyte and Taiwan warm current species in the East China Sea. Oceanogr Res 38:38–48
Zhao Y, Yu Z, Song X, Cao X (2009) Biochemical compositions of two dominant bloom-forming species isolated from the Yangtze River Estuary in response to different nutrient conditions. J Exp Mar Biol Ecol 368:30–36
Zohdi E, Abbaspour M (2019) Harmful algal blooms (red tide): a review of causes, impacts and approaches to monitoring and prediction. Int J Environ Sci Technol 16:1789–1806

Publisher's Note